Available online at www.sciencedirect.com
ScienceDirect
Polymer 47 (2006) 6745–6758
polymer
www.elsevier.com/locate/polymer

# On the characterization of tensile creep resistance of polyamide 66 nanocomposites. Part II: Modeling and prediction of long-term performance

Jing-Lei Yang [a], Zhong Zhang [b,*], Alois K. Schlarb [a], Klaus Friedrich [a]

[a] *Institute for Composite Materials, University of Kaiserslautern, 67663 Kaiserslautern, Germany*
[b] *National Center for Nanoscience and Technology, No. 2, 1st North Street Zhongguancun, 100080 Beijing, PR China*

Received 10 January 2006; received in revised form 24 July 2006; accepted 24 July 2006

**Abstract**

The Part I of this study [Yang JL, Zhang Z, Schlarb AK, Friedrich K. Polymer 2006;47:2791–801] provided systematic experiments and general discussions on the creep resistance of polyamide 66 nanocomposites. To promote these works, here we present some modeling and prediction attempts in order to further understand the phenomena and mechanisms. Both a viscoelastic creep model named Burgers (or four-element model) and an empirical method called Findley power law are applied. The simulating results from both models agree quite well with the experimental data. An additional effort is conducted to understand the structure–property relationship based on the parameter analysis of the Burgers model, since the variations in the simulating parameters illustrate the influence of nanofillers on the creep performance of the bulk matrix. Moreover, the Eyring stress-activated process is taken into account by considering the activation volume. Furthermore, in order to predict the long-term behavior based on the short-term experimental data, both the Burgers and Findley models as well as the time–temperature superposition principle (TTSP) were employed. The predicting capability of these modeling approaches is compared and the Findley power law is preferred to be adopted. Master curves with extended time scale are constructed by applying TTSP to horizontally shift the short-time experimental data. The predicting results confirm the enhanced creep resistance of nanofillers even at extended long time scale.


*Keywords:* Creep modeling; Creep prediction; Polymer nanocomposites

## 1. Introduction

In view of the fact that nanomaterials as fillers become the state-of-the-art in materials science, numerous studies have been carried out and many improved mechanical properties have been achieved with incorporations of nanofillers into polymer matrices [1]. However, the complex performance of polymer nanocomposites can only be understood deeply by combining experimental studies with effective modeling. Therefore, modeling and simulation of polymer-based nanocomposites have become an essential issue due to the demand for developing these materials to potential engineering applications. In the past years many modeling studies have been carried out. Most of them have focused on the prediction of elastic modulus, interfacial bonding or load transfer for either carbon nanotubes [2–5] or spherical nanoparticles-filled polymers [6–10].

Moreover, for the long period of loading, e.g., creep or fatigue (must be taken into account in design, especially in aviation and automotive applications [11,12]), it is usual that the material must remain in service for an extended period of time, normally longer than it is practical to run creep experiments on the materials to be employed. Therefore, it is necessary to extrapolate the information obtained from relatively short-term laboratory creep tests in order to predict the probable behavior in service. However, to the best knowledge of the authors, no analytical and prediction work has been reported on the creep behavior of nanoparticle/thermoplastic composites up to now. Recent work of Sarvestani and Picu [13] proposed a network model to simulate the viscoelastic

* Corresponding author.
*E-mail address:* zhong.zhang@nanoctr.cn (Z. Zhang).

0032-3861/$ - see front matter © 2006 Elsevier Ltd. All rights reserved.
doi:10.1016/j.polymer.2006.07.060

**Nomenclature**

| | |
|---|---|
| $a_T$ | temperature shift factor |
| $C_1$, $C_2$ | constants in Eq. (13) |
| $E_{tensile}$ | Young's modulus from static tensile test |
| $E_K$ | modulus of the Kelvin spring in the Burgers model |
| $E_M$ | modulus of the Maxwell spring in the Burgers model |
| $\Delta H$ | activation energy |
| $k$ | Boltzmann constant |
| $n$ | power in the Findley power law |
| R | universal gas constant |
| $t$ | time |
| $T$ | absolute temperature |
| $T_g$ | glass transition temperature |
| $T_{ref}$ | reference temperature |

*Greek symbols*

| | |
|---|---|
| $\varepsilon_B$ | strain of the Burgers model |
| $\varepsilon_F$ | strain of the Findley power law |
| $\varepsilon_{F0}$ | time-independent strain in the Findley power law |
| $\varepsilon_{F1}$ | time-dependent term in the Findley power law |
| $\varepsilon_K$ | strain of the Kelvin unit in the Burgers model |
| $\varepsilon_{M1}$ | strain of the Maxwell spring in the Burgers model |
| $\varepsilon_{M2}$ | strain of the Maxwell dashpot in the Burgers model |
| $\dot{\varepsilon}_{II}$ | fitted strain rate from the secondary creep stage |
| $\dot{\varepsilon}_B$ | strain rate of the Burgers model |
| $\dot{\varepsilon}_E$ | strain rate of Eyring creep process |
| $\dot{\varepsilon}_{E0}$ | constant pre-exponential factor in Eq. (9) |
| $\dot{\varepsilon}_F$ | strain rate of the Findley power law |
| $\dot{\varepsilon}_K$ | strain rate of the Kelvin dashpot in the Burgers model |
| $\dot{\varepsilon}_{M2}$ | strain rate of the Maxwell dashpot in the Burgers model |
| $\eta_K$ | viscosity of the Kelvin dashpot in the Burger model |
| $\eta_M$ | viscosity of the Maxwell dashpot in the Burger model |
| $\sigma$ | stress applied in creep test |
| $\sigma_0$ | initial stress applied in tensile creep test |
| $\tau$ | retardation time of the Kelvin unit in the Burgers model |
| $v$ | activation volume in stress-activated Eyring process |

behavior of nanoparticle/polymers. The rheology and shear viscosity of nanocomposites were simulated by taking into account the important roles of the lifetime of the polymer–filler junctions and the network of bridging segments. More recently Blackwell and Mauritz [14] reported the shear creep behavior of a sulfonated poly(styrene-*b*-ethylene/butylene-*b*-styrene) (sSEBS)/silicate nanocomposite, the experimental data of which could be satisfactorily simulated by using a modified Burgers creep model. However, the shear creep experiments were conducted by using a dynamic thermal analyzer (DMA) within a very short time of 30 min and no further explanations and discussions of the results were given. Although the analytical work on the fluid viscoelasticity and the very short time creep of the nanocomposites presented some valuable points, some detailed explorations were needed for practical applications.

In our previous experimental studies, the creep behavior of a semicrystalline thermoplastic polyamide 66 (PA66) nanocomposites was systematically carried out at various temperatures and different stress levels [1,15]. The creep deformation and the creep rate of the matrix were reduced to different extents by the addition of various nanofillers. Significantly improved creep resistance broadens the research scope and, together with the enhanced crack initiation fracture toughness [16,17], will certainly extend the potential applications of nanocomposites. In addition, considering the design of nanocomposites for engineering applications, modeling and predicting work becomes a key issue. Thus, in the present study the modeling study based on experimental data by using traditional creep models [19,20] is conducted. An attempt to understand the structure–property relationship is carried out based on the parameter analysis of the Burgers model, since the variations in the simulating parameters illustrate the influence of nanofillers on the creep performance of the bulk matrix. Moreover, the Eyring stress-activated process [21] is taken into account by considering the activation volume. Furthermore, in order to predict the long-term behavior based on the short-term experimental data, both the Burgers and Findley models as well as the time–temperature superposition principle (TTSP) [21] were employed. Master curves with extended time scale are constructed by applying TTSP to horizontally shift the short-time experimental data. The predicting results confirm the enhanced creep resistance of nanofillers even at extended long time scale.

## 2. Theoretical background

### 2.1. Creep models

#### 2.1.1. Burgers model

Among the numerous viscoelastic creep models, Burgers or four-element model [19,21] is widely used to analyze the viscoelasticity of materials, as illustrated in Fig. 1 with a Maxwell and a Kelvin unit connected in series. The constitutive equation for a Burgers model can be derived by considering the strain response under constant stress of each coupled element in series as depicted in Fig. 1. The total strain $\varepsilon_B$ at time $t$ is a sum of the strains in these three elements, where the spring and dashpot in the Maxwell model are considered as two elements, thus:

$$\varepsilon_B = \varepsilon_{M1} + \varepsilon_{M2} + \varepsilon_K \quad (1)$$

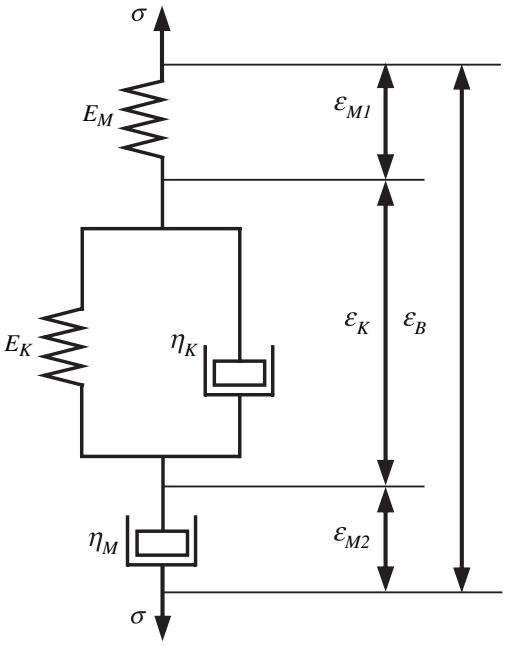


Fig. 1. Schematic diagram of Burgers model.

where the subscripts B, M, and K indicate Burgers model, Maxwell and Kelvin elements, respectively; $\varepsilon_{M1}$, $\varepsilon_{M2}$, and $\varepsilon_K$ are the strains of the Maxwell spring, Maxwell dashpot, and Kelvin unit, respectively. Considering the constitutive relations of the elements and the initial conditions at $t=0$, the creep behavior of Burgers model can be finally obtained as follows (see Ref. [21] for detailed deduction)

$$\varepsilon_B = \frac{\sigma_0}{E_M} + \frac{\sigma_0}{E_K}\left(1 - e^{-t/\tau}\right) + \frac{\sigma_0}{\eta_M} t \tag{2}$$

where $E_M$ and $\eta_M$ are the modulus and viscosity of the Maxwell spring and dashpot, respectively; $E_K$ and $\eta_K$ are the modulus and viscosity of the Kelvin spring and dashpot, respectively; $\sigma_0$ is the initially applied stress; $\tau = \eta_K/E_K$ is the retardation time taken to produce 63.2% or $(1-e^{-1})$ of the total deformation in the Kelvin unit.

The creep characteristics of Burgers model shown in Eq. (2) can be depicted as follows. The first term is constant and describes the instantaneous elastic deformation; the second one is delayed elasticity of the Kelvin unit and dominant in the earliest stage of creep, but soon goes to a saturation value close to $\sigma_0/E_K$; the viscous flow then increases nearly linearly in the third term after a sufficient long time period of loading.

Differentiating Eq. (2) yields the creep rate $\dot{\varepsilon}_B$ of Burgers model

$$\dot{\varepsilon}_B = \frac{\sigma_0}{\eta_M} + \frac{\sigma_0}{\eta_K} e^{-t/\tau} \tag{3}$$

At sufficient long time scale, the creep rate reaches asymptotically to a constant value

$$\dot{\varepsilon}_B(\infty) = \frac{\sigma_0}{\eta_M} \tag{4}$$

The Burgers model, which includes the essential elements, can be applied satisfactorily to model the practical behaviors of viscoelastic materials. The material parameters $E_M$, $\eta_M$, $E_K$, and $\eta_K$ can be simulated from the experimental data. The variation of the simulated parameters will constitutively show the effect of nanofillers.

### 2.1.2. Findley power law

Considering the creep curves for many polymers are similar to those of some metals, some authors proposed several empirical mathematical models to represent the creep data of plastics. Among them Findley et al. [19] brought forward the following empirical power equation, which could describe the creep behavior of many polymers with good accuracy over a wide time scale:

$$\varepsilon_F = \varepsilon_{F0} + \varepsilon_{F1} t^n \tag{5}$$

or in terms of creep compliance $J_F$:

$$J_F = J_{F0} + J_{F1} t^n \tag{6}$$

where the subscript F indicates the parameters associated with the Findley power law; $n$ is a constant independent of stress and generally less than one; $\varepsilon_{F0}$ and $J_{F0}$ are the time-independent strain and compliance, respectively; $\varepsilon_{F1}$ and $J_{F1}$ are the coefficients of time-dependent terms; $\varepsilon_{F0}$ and $\varepsilon_{F1}$ are functions of stress and environmental variables including temperature and moisture, etc. The creep time $t$ may be taken to represent a dimensionless time ratio $t/t_0$, where $t_0$ is unit time. In this case $\varepsilon_{F1}$ has the dimension of strain, i.e., dimensionless. When $t$ is taken to have the dimension of time then $\varepsilon_{F1}$ has the dimension of $(\text{time})^{-n}$.

Rearranging Eq. (5) and taking logarithms yields

$$\log(\varepsilon_F - \varepsilon_{F0}) = \log \varepsilon_{F1} + n \log t \tag{7}$$

Thus, when $\log(\varepsilon_F - \varepsilon_{F0})$ is plotted vs. $\log t$ a straight line with slope $n$ and intercept at unit time of $\varepsilon_{F1}$ is predicted. If $n$ is independent of stress and state of stress, curves under various stresses should be in parallel.

Differentiating Eq. (5) and the creep rate $\dot{\varepsilon}_F$ of the Findley power law yields

$$\dot{\varepsilon}_F = \frac{n\varepsilon_{F1}}{t^{1-n}} \tag{8}$$

Here when the creep time $t \to \infty$, it results to $\dot{\varepsilon}_F(\infty) \to 0$. This case is available for the polymers that do not exhibit a pronounced secondary creep stage, especially for the case under low stress level.

The power law has been widely applied to express stress–strain–time relationship for viscoelastic materials [19] and considered in the current study.

## 2.2. Activation volume

The Burgers model can provide an approximate description of the linear viscoelastic behavior. The deformation of

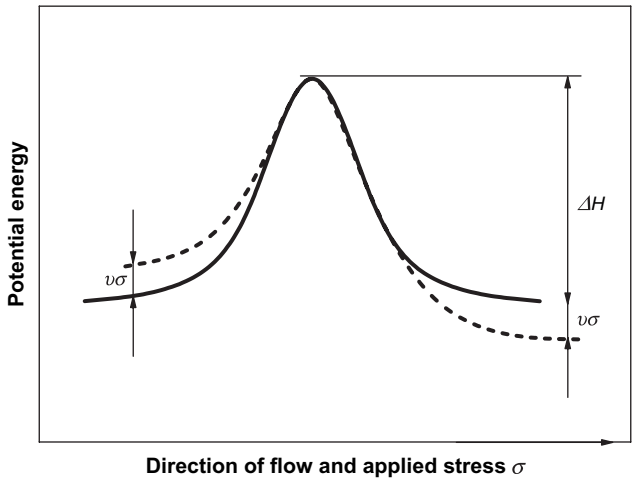


Fig. 2. The Eyring model showing a stress activated process for creep.

a polymer was also considered as an activated rate process involving the motion of segments of chain molecules over potential barriers, and modified the standard linear solid so that the movement of the dashpot was governed by the activated process. As illustrated in Fig. 2, the Eyring model is introduced here due to its useful parameter of activation volume that may provide an indication of the underlying molecular mechanisms. The activated rate process may also provide a common basis for the discussion of creep behavior.

The creep rate of a stress-activated Eyring dashpot is given by [21]:

$$\dot{\varepsilon}_{\mathrm{E}} = \dot{\varepsilon}_{\mathrm{E0}} \mathrm{e}^{-\frac{\Delta H}{kT}} \sinh\left(\frac{\upsilon\sigma}{kT}\right) \tag{9}$$

where the subscript E indicates an Eyring process; $\dot{\varepsilon}_{\mathrm{E0}}$ is a constant pre-exponential factor; $\Delta H$ represents the energy barrier height; $\upsilon$ is the activation volume for the molecular event; $k$, $\sigma$ and $T$ are Boltzmann constant, applied stress and absolute temperature, respectively. Under high stress levels ($\sigma > 3kT/\upsilon$) the hyperbolic sine term can be approximated to $(1/2)\exp(\upsilon\sigma/kT)$. Therefore, Eq. (9) can be simplified as:

$$\dot{\varepsilon}_{\mathrm{E}} = \frac{1}{2}\dot{\varepsilon}_{\mathrm{E0}} \mathrm{e}^{-((\Delta H - \upsilon\sigma)/kT)} \tag{10}$$

It follows that:

$$\frac{\partial \ln \dot{\varepsilon}_{\mathrm{E}}}{\partial \sigma} = \frac{\upsilon}{kT} \tag{11}$$

Finally, approximate value of the activation volume for the tested specimens can be obtained from the high stress levels, e.g., in the current study $\sigma_1 = 30$ MPa and $\sigma_2 = 40$ MPa, together with the corresponding steady creep rates under those loads,

$$\upsilon = kT\frac{(\ln \dot{\varepsilon}_{\mathrm{E}})_{\sigma_2} - (\ln \dot{\varepsilon}_{\mathrm{E}})_{\sigma_1}}{\sigma_2 - \sigma_1} \tag{12}$$

The variation of the activation volume will show the effect of nanofillers on the matrix.

### 2.3. Time–temperature superposition principle (TTSP)

Many experiments of creep performance have been directed at making long-term creep predictions from short-time creep tests. The most acceptable methods for realizing this involve using TTSP, which implies that the viscoelastic behavior at one temperature can be related to that at another temperature by a change in the time scale only. The detailed procedure is that creep tests performed at high temperatures for short times can mimic the creep behaviors performed at low temperatures over long time scale [21,22].

In the current investigation, creep experiments of PA66 and nanocomposites were carried out at three temperatures. The creep data were then shifted horizontally along the logarithmic time axis until they overlapped to form one continuous master curve, which can be used to predict creep performance over long time scale. If a reference temperature $T_{\mathrm{ref}}$ other than the glass transition temperature is selected, the shift factor $a_{\mathrm{T}}$ can be calculated by means of WLF Eq. [21]:

$$\log a_{\mathrm{T}} = -\frac{C_1(T - T_{\mathrm{ref}})}{C_2 + (T - T_{\mathrm{ref}})} \tag{13}$$

where $C_1$ and $C_2$ are constants dependent on the nature of the material. Furthermore, the temperature dependent shift factor $a_{\mathrm{T}}$ is related to the activation energy $\Delta H$ as follows:

$$\log a_{\mathrm{T}} = \frac{\Delta H}{2.303\mathrm{R}}\left(\frac{1}{T} - \frac{1}{T_{\mathrm{ref}}}\right) \tag{14}$$

where R is the universal gas constant. The activation energy can be obtained from the slope of the curve of $\log a_{\mathrm{T}}$ against $1/T$. The variation of $\Delta H$ shows the different effects of nanofillers on the matrix.

## 3. Materials and experimental procedure

As introduced in the Part I of this study [1], a widely used polyamide 66 (PA66) was chosen as matrix. For nanofillers, titanium dioxide particles with diameters of 300 nm and 21 nm were chosen. $TiO_2$ particles (21 nm) treated with octylsilane to achieve a hydrophobic surface were considered as well. Additionally, nanoclay was also selected. The volume content of nanofillers was chosen as a constant of 1%. The details and designations of the materials were given in Table 1 as well.

Uniaxial tensile creep experiments were preformed using a Creep Rupture Test Machine with double lever system (Coesfeld GmbH, Model 2002). The elaborate experimental procedure was given in Part I [1] and the creep conditions were listed in Table 1. The creep behavior of the materials was observed within 200 h, which covered the primary and part of the secondary creep stage. Modeling procedures were conducted based on these experimental data.

Table 1
The details of the materials used in this study

| Specimen code | PA66 | PA/300 | PA/21-SM | PA/21 | PA/Clay |
|---|---|---|---|---|---|
| Nanofillers | – | 300 nm-$TiO_2$ | Surface treated with octylsilane 21 nm-$TiO_2$ | 21 nm-$TiO_2$ | 100–500 nm × 1 nm clay layer |
| Manufacture code | Zytel 101 | Kronos 2310 | Aeroxide T805 | Aeroxide P25 | Nanofil 919 |
| wt% (1 vol%) of filler | 0 | 3.4 | 3.4 | 3.4 | 1.6 |

Creep experimental condition – temperatures: 23 °C, 50 °C, 80 °C; stress levels: 20 MPa, 30 MPa, 40 MPa.

## 4. Modeling results and discussions

The experimental data were simulated by using the Non-Linear Curve Fit function in OriginPro. The functions of the Burgers model with four undetermined parameters and the Findley power law with three undetermined parameters were defined in OriginPro. The initial values of the parameters were carefully chosen to make the calculation asymptotically convergent to experimental data. Otherwise the bad initial values led to non-convergent result and made the simulation fail. The simulation was performed by the program using a least square approximation procedure and the parameters were brought for further discussions.

### *4.1. Modeling parameters of Burgers model and structure–property relationship*

The representative experimental curves of creep strain vs. creep time of the specimens tested at 50 °C under different stress levels are presented in Fig. 3. The simulated curves by using Burgers model are drawn in solid lines. It could be seen that the modeling curves showed a satisfactory agreement with the experimental data under each condition. The complete modeling parameters of the samples listed in Table 2 are discussed in the following subsections.

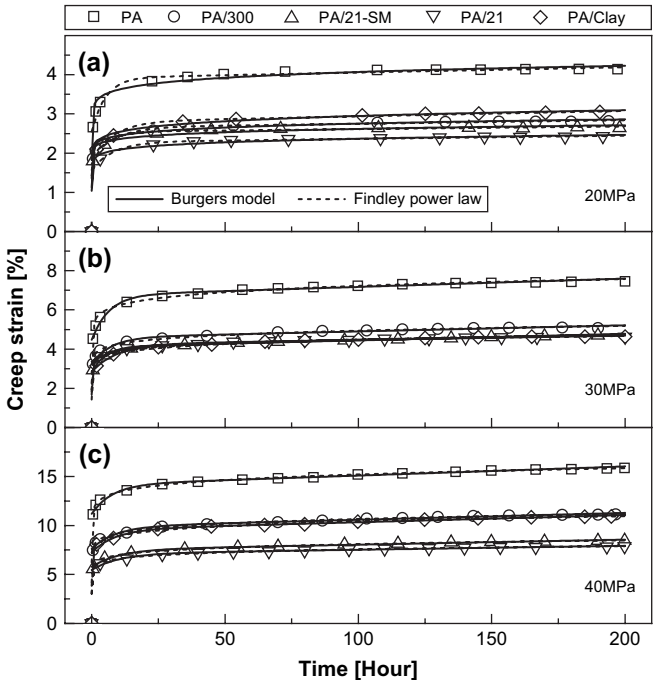


Fig. 3. Modeling results of the representative experimental creep data obtained at 50 °C under (a) 20 MPa, (b) 30 MPa, and (c) 40 MPa.

#### *4.1.1. Time-independent elasticity $E_M$*

According to the constitutive Eq. (2), it is shown that the modulus $E_M$ of the Maxwell spring determined the instantaneous elastic creep strain, which could be immediately recovered on the removal of stress. In general, the composites showed the higher values of $E_M$ compared to neat matrix under each condition. Among the composites PA/21 behaved with the highest elasticity, and then PA/21-SM, and PA/300 and PA/Clay in the close lowest level, which depicted that smaller nanoparticles without surface modification were much more effective in reinforcing the elasticity of polymer matrix, and that nanoclay layers, although with a different structure from nanoparticles, performed a similar resulting reinforcement as large nanoparticles in elasticity, as shown in Table 2. However, the different variations of $E_M$ of the tested materials under various loads and temperatures illustrated the diverse reinforcing characteristics of nanofillers.

$E_M$ of each specimen showed a decreasing tendency with temperature, which was easy to understand that the bulk materials became soft at elevated temperatures and the stiffness was thus decreased with diminished instantaneous modulus. However, stress dependent $E_M$ was much more complicated. Additionally, to deeply understand the relationship between the parameterized model and the real structure of the materials, a representative configuration of the nanoparticle/polymer composites was schematically presented in Fig. 4. Some essential parts including crystallized and amorphous polymer, polymer–filler junction, intercrystalline tie molecule, and segment and crystalline bridging were considered. These elements exhibited different behaviors under various stresses and temperatures.

At 23 °C, $E_M$ was non-sensitive to the load within the observed range except for PA under 40 MPa, where an obvious drop in $E_M$ occurred due to the bad ability of load bearing. The performance was consistent with the fact that the short-time response at room temperature (RT), as determined, for example, from the one-hour isochronous modulus, was linear, i.e., creep strain proportional to stress level, which was conformably shown in Fig. 5(a). In addition, the range of stress exhibiting linear behavior is broadened by the addition of nanofillers. Among the tested materials, $E_M$ showed comparatively small changes between neat matrix PA66 and the

Table 2
The simulated parameters of the Burgers model and the activation volume $\upsilon$ at higher stress levels

| | Sample | $\sigma_0$ (MPa) | $E_{tensile}$ (MPa) | $E_M$ (MPa) | $E_K$ (MPa) | $\eta_M$ (GPa h) | $\eta_K$ (GPa h) | $\tau$ (h) | $\upsilon$ (nm$^3$) |
|---|---|---|---|---|---|---|---|---|---|
| 23 °C | PA66 | 20 | 2280 | 3709 | 16,617 | 889 | 236 | 14.2 | 0.590 |
| | | 30 | | 3653 | 8673 | 991 | 113 | 13.1 | |
| | | 40 | | 2490 | 1616 | 404 | 23.7 | 14.7 | |
| | PA/300 | 20 | 2650 | 1909 | 16,665 | 1270 | 253 | 15.2 | 0.474 |
| | | 30 | | 2536 | 6580 | 1311 | 102 | 15.5 | |
| | | 40 | | 2647 | 2646 | 681 | 38.1 | 14.4 | |
| | PA/21-SM | 20 | 2270 | 3509 | 19,642 | 2394 | 315 | 16 | 0.425 |
| | | 30 | | 3204 | 8514 | 1928 | 185 | 21.7 | |
| | | 40 | | 3442 | 3584 | 896 | 60 | 16.8 | |
| | PA/21 | 20 | 2760 | 4348 | 22,815 | 1819 | 272 | 11.9 | 0.361 |
| | | 30 | | 4267 | 8713 | 1841 | 183 | 20.9 | |
| | | 40 | | 3708 | 4652 | 1033 | 91.7 | 19.7 | |
| | PA/Clay | 20 | 2770 | 3344 | 24,411 | 1330 | 406 | 16.6 | 0.536 |
| | | 30 | | 4418 | 7371 | 1301 | 105 | 14.3 | |
| | | 40 | | 3130 | 3900 | 696 | 78.1 | 20 | |
| 50 °C | PA66 | 20 | 1470 | 784 | 1458 | 1487 | 76.4 | 5.24 | 0.418 |
| | | 30 | | 671 | 1317 | 706 | 85.6 | 6.5 | |
| | | 40 | | 357 | 1348 | 429 | 10.4 | 7.7 | |
| | PA/300 | 20 | 1690 | 1039 | 2718 | 2248 | 25.3 | 9.3 | 0.426 |
| | | 30 | | 918 | 2269 | 956 | 16.6 | 7.31 | |
| | | 40 | | 525 | 1773 | 570 | 16 | 9.04 | |
| | PA/21-SM | 20 | 2020 | 1163 | 2421 | 2963 | 13.6 | 5.6 | 0.234 |
| | | 30 | | 1068 | 2295 | 906 | 11.4 | 4.98 | |
| | | 40 | | 692 | 2302 | 774 | 23.4 | 10.2 | |
| | PA/21 | 20 | 1820 | 1274 | 2809 | 2446 | 22.8 | 8.13 | 0.279 |
| | | 30 | | 991 | 2567 | 1169 | 16.3 | 6.35 | |
| | | 40 | | 732 | 2418 | 988 | 24.9 | 10.3 | |
| | PA/Clay | 20 | 1810 | 1087 | 2083 | 1455 | 17.2 | 8.28 | 0.467 |
| | | 30 | | 1059 | 2242 | 1043 | 19.8 | 8.85 | |
| | | 40 | | 551 | 1712 | 544 | 15.2 | 8.88 | |
| 80° C | PA66 | 20 | 860 | 400 | 1835 | 1675 | 7.34 | 4 | 0.818 |
| | | 30 | | 284 | 1336 | 818 | 6.77 | 5.1 | |
| | | 40 | | 156 | 232 | 207 | 0.75 | 3.2 | |
| | PA/300 | 20 | 1030 | 584 | 2714 | 3239 | 14.9 | 5.5 | 1.147 |
| | | 30 | | 412 | 2120 | 1772 | 11.06 | 5.22 | |
| | | 40 | | 181 | 586 | 322 | 5.65 | 9.65 | |
| | PA/21-SM | 20 | 980 | 680 | 2599 | 2146 | 9.85 | 3.79 | 0.956 |
| | | 30 | | 470 | 2262 | 2179 | 9.55 | 4.22 | |
| | | 40 | | 290 | 1128 | 573 | 12.3 | 10.9 | |
| | PA/21 | 20 | 1060 | 707 | 2987 | 3652 | 19 | 6.37 | 0.371 |
| | | 30 | | 465 | 2360 | 1976 | 14.3 | 6.08 | |
| | | 40 | | 289 | 1428 | 793 | 14.2 | 9.97 | |
| | PA/Clay | 20 | 1050 | 602 | 1841 | 1997 | 6.17 | 3.35 | 0.983 |
| | | 30 | | 407 | 1753 | 1239 | 9.32 | 5.32 | |
| | | 40 | | 190 | 619 | 319 | 7.47 | 12.1 | |

$E_{tensile}$ is the Young's modulus obtained from the quasi-static tensile experiments [1]. The activation volume $\upsilon$ is calculated under high stress levels (30–40 MPa).

nanocomposites, which provided the fact that the instantaneous elasticity was not much altered by the addition of nanofillers. The instantaneous elasticity $E_M$ was reasonably corresponding to the elasticity of the crystallized polymer or regular chain folds, which took the immediate load due to high stiffness compared to amorphous polymers, as illustrated in Fig. 4. However, although the crystalline morphology was changed by the addition of nanofillers the crystallinity of each specimen was not obviously altered [17,18], which implied the load bearing parts were not of great difference between neat matrix and nanocomposites.

At 50 °C, with increasing stress levels $E_M$ of each specimen was decreased slightly from 20 MPa to 30 MPa and significantly reduced under high stress of 40 MPa. It was reasonable to believe that there existed a threshold of linear viscoelasticity near the stress of 30 MPa in the short-time response, which was also consistent with the one-hour isochronous stress–strain relationship in Fig. 5(b). Among the observed specimens, the nanocomposites behaved with much better elasticity compared to pure matrix, showing an effective reinforcement by the addition of nanofillers near the glass transition temperature. $E_M$ was increased with decreasing particle size under each stress level while the value of PA/21-SM was very close to that of PA/21, depicting at 50 °C nanoparticles with surface modification had no obvious contribution to the elasticity of the bulk material compared to non-surface

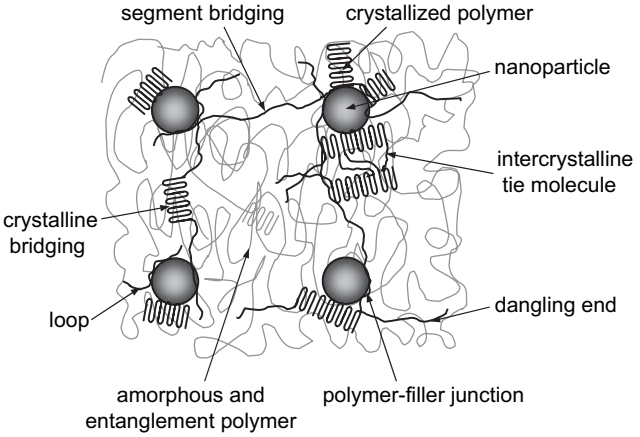


Fig. 4. Schematic representative structure of nanoparticle–semicrystalline polymer composites. (Based on the assumption that the particles with 1 vol% have a diameter of 20 nm, the polymer chains have a diameter of 1 nm, the interparticle distance is 60 nm, and the crystal lamellae thickness is roughly 10 nm.)

modified particles. $E_M$ of PA/Clay was a little bit higher than that of PA/300, showing the resulting reinforcing effectiveness of nanoclay layers was of the similar level to that of large nanoparticles. Near the glass transition temperature polymer chains began to become active. Consequently, the stiffness of bulk material was decreased, which resulted in the low value of $E_M$ compared to that at room temperature. According to the dependency of $E_M$ on stress, it might be considered that the elastic limit of each tested material was slightly lower than 30 MPa, below which a minute change of $E_M$ occurred while a large fall-off under 40 MPa was observed. As described in the former study [1], the amount of small particles in unit volume matrix was higher than that of large ones by several orders of magnitude. Small particles with bridging segments could form a much huge and dense network compared to large ones. This network, together with the crystallized polymer chains, could enhance the capability to bear load, markedly at elevated temperatures. In the case of PA/Clay, nanoclay layers could bear load due to the large aspect ratio of individual platelet while discounted by the slippage of stacks and large amount of unexfoliated layers. Hence, the resulting $E_M$ of PA/Clay was very close to that of PA/300.

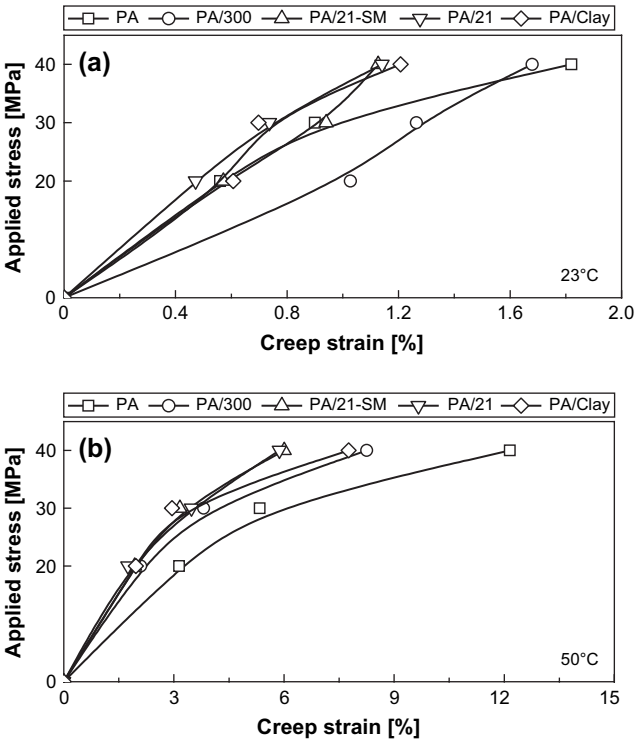


Fig. 5. The one-hour isochronous stress–strain relationship of PA and nanocomposites at (a) 23 °C and (b) 50 °C.

At temperature above $T_g$, i.e., 80 °C, $E_M$ of each specimen was clearly decreased with increasing stress, showing a non-elastic deformation in the short-time response due to easy viscous flow of bulk materials. The nanocomposites possessed high elasticity under each stress level, which indicated that nanofillers were capable to enhance the elasticity of polymer matrix even at elevated temperatures. PA/21-SM and PA/300 provided very close elasticity to PA/21 and PA/Clay, respectively. The similar resulting performance illustrated again that at elevated temperature surface modification had no apparent contribution to the elasticity of bulk materials. Because of enhanced mobility of amorphous chains and even chain folds at very high temperature the stiffness of the bulk materials was significantly decreased with very low $E_M$. The limit of elasticity of each material was somewhat below 20 MPa since $E_M$ was clearly dependent on the stress observed from 20 MPa to 40 MPa. The network of small particles was much effective to enhance the elasticity compared to that of large ones and clay layers. Due to the same causes as that at 50 °C mentioned above, PA/300 and PA/Clay exhibited similar $E_M$ but at lower level.

### *4.1.2. Retardant elasticity $E_K$ and viscosity $\eta_K$*

The retardant elasticity $E_K$ and viscosity $\eta_K$ of each specimen showed the similar dependency to temperature, decreased with increasing temperature. It could be alternatively described that the deformation of the Kelvin unit of each material was increased with increasing temperature. However, the stress dependent $E_K$ showed a great different scenario from the instantaneous elasticity $E_M$. The time-dependent $E_K$ and $\eta_K$ in the Kelvin unit might be associated with the stiffness and viscous or orientated flow of amorphous polymer chains in short term, respectively.

At room temperature, $E_K$ and $\eta_K$ were considerably decreased with increasing load, showing high stress dependency. This indicated a fact that the materials with relatively high bulk modulus deformed very small under low stress, which showed the Kelvin unit behaved with extremely high modulus and very difficult viscous flow. With increasing stress, the orientation movement of amorphous chains including elastic deformation and viscous flow became exaggerative, resulting in the reduced $E_K$ and $\eta_K$. The consistent change of $E_K$ and $\eta_K$ with stress led to a nearly constant retardant time $\tau$ for each specimen, as illustrated in Table 2.

In the temperature range around the $T_g$, amorphous polymer became much active and was promptly oriented in a short-term

period once the stress loaded. The polymer chains thereafter lied in a high potential energy site due to orientational hardening [22]. However, the Kelvin unit could not be reorientated further in the observed time scale due to relatively low stress, which resulted in nearly constant $E_K$ and $\eta_K$ of each specimen except for PA66 under 40 MPa, where an obvious viscous flow occurred. And the retardant time $\tau$ was also kept constant.

Since the mobility of amorphous polymer at 80 °C was much more active, the reorientation of amorphous polymer chains was greatly different from the case at $T_g$. According to the obtained parameters under various stress levels, there existed a threshold stress near 30 MPa, below which the reorientation of amorphous polymer was not able to be activated with nearly constant $E_K$, $\eta_K$, and $\tau$, whereas, above which the Kelvin elements were deformed with advanced reorientation including significant plastic deformation and viscous flow of crystalline and amorphous chains and reduced retardant time $\tau$.

It should be pointed out that all nanofillers showed reinforcing effectiveness on the Kelvin unit. For the observed fillers the small-sized particles with tridimensional network in matrix are most effective to retard the deformation of the Kelvin elements. Generally, PA/21-SM was slightly weakened because of the deteriorated interface strength caused by modified surfaces of particles. PA/300 and PA/Clay behaved with similar resulting performances probably due to their close amount of fillers in unit volume bulk material.

*4.1.3. Permanent viscous flow $\eta_M$*

On the basis of the discussion of the instantaneous and time-dependent recoverable components, which showed enhancement to some extent by the presence of nanofillers, hereafter we would like to provide an analysis of a more important parameter $\eta_M$, which represented the irrecoverable creep and was a factor of several to tens higher than $\eta_K$, and very sensitive to stress except for at 23 °C below 30 MPa, as compared in Fig. 6 showing stress influence and in Fig. 7 showing temperature effect. A more detailed understanding of $\eta_M$ was therefore necessarily carried out.

From Table 2 it could be seen that $\eta_M$ was not strongly dependent on temperature, unlike $E_M$, $E_K$ and $\eta_K$. It could be considered that $\eta_M$ was associated with the damage from crystallized polymer or oriented noncrystalline regions, such as the pulling out of chain folds by a crystal slip process and the breaking of an intercrystalline tie molecule, and the irreversible deformation from amorphous regions, such as the breaking of bridging segments, disengaged junction between fillers and polymer chains and the pulling out of a chain entanglement, as illustrated in Fig. 4. Hereby a stress-activated Eyring process was adopted as introduced in the above section. The activation volume under higher stress levels was given in Table 2 and would be discussed in the following analysis.

At room temperature, $\eta_M$ was not sensitive to the stress below 30 MPa while apparently decreased under 40 MPa, as clearly provided in Fig. 6(a), which showed the damage of crystallized polymer was of the same level under low stress, however, the damage became serious due to the high stress reached or exceeded the elastic limit of the crystallized parts.

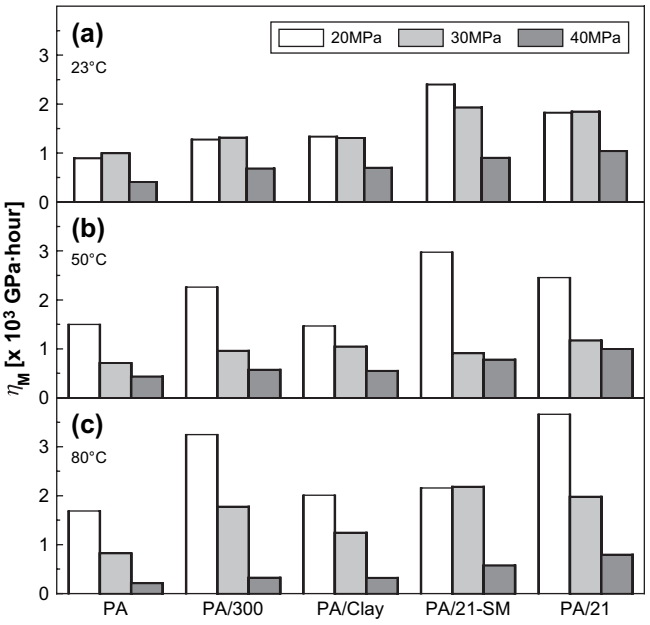


Fig. 6. The relationship of $\eta_M$ and applied stress at (a) 23 °C, (b) 50 °C, and (c) 80 °C, respectively.

The activation volume of each specimen was in a range from 0.36 nm$^3$ to 0.6 nm$^3$. Under low stress the Eyring process was probably associated with the separation of bridging segment or crystalline, while under 40 MPa the activated process was corresponding to the large plastic deformation of crystallized polymer, as shown in Fig. 4. The enhanced deformation resistance of Eyring dashpot was obtained due to the presence of nanofillers, which changed the crystalline morphology of matrix and formed a three-dimensional stiff structure together with crystallized molecules [18]. Consequently, PA/21 behaved with best performance among the composites and then

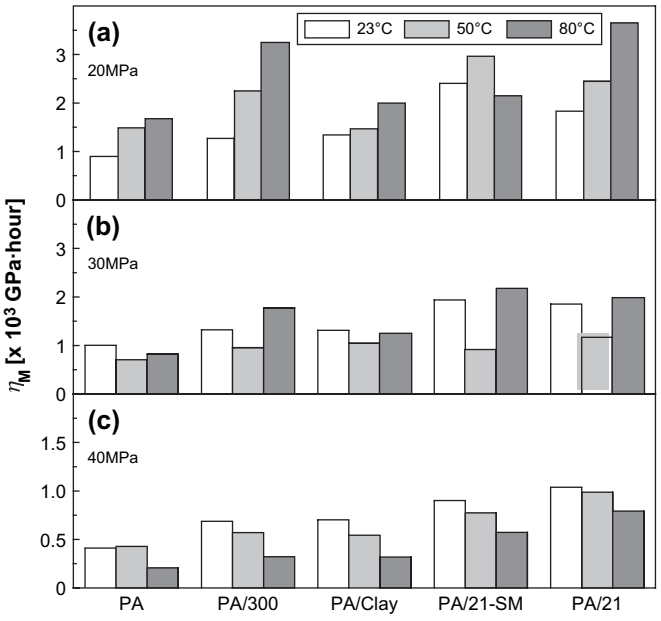


Fig. 7. The relationship of $\eta_M$ and temperature under (a) 20 MPa, (b) 30 MPa, and (c) 40 MPa.

PA/21-SM. Large particles and nanoclay layers exhibited similar resulting performance.

In the case of 50 °C, $\eta_M$ was significantly decreased with increasing stress, reflecting the fact of increment of irrecoverable deformation, as shown in Fig. 6(b). The activation volume of each specimen was smaller than that at 23 °C, indicating a much local molecular process near $T_g$, such as the breaking of an intercrystalline tie molecule and detaching of polymer–filler junction, as illustrated in Fig. 4. The irreversible creep strain was diminished by the addition of nanofillers, which enhanced the immobility of polymer chains and resulted in a much local Eyring process in the meantime. PA/21 behaved with the least permanent deformation while PA/21-SM showed the smallest activation volume due to a uniform dispersion of particles with surface modification. Nanoclay layers had no obvious advantage over large nanoparticles on affecting the molecular process.

A similar scenario occurring at 80 °C compared to that at 50 °C that $\eta_M$ was considerably decreased with increasing stress, is shown in Fig. 6(c). However, an interesting phenomenon was presented that the activation volume of each specimen was the largest among the observed temperatures, probably indicating a different stress-activated process at 80 °C. Polymer chains were highly thermally activated at this temperature. Large deformation of crystallized polymer such as the pulling out of chain folds by a crystal slip process and the irreversible transition of amorphous polymer such as the pulling out of chain entanglement and orientation crystallization under external stress [18,24], were relatively large scale cooperation of deformation. While the stress-activated process could partially be resisted by the appearance of nanofillers, which acted as blocking sites to retard or restrict the slippage of crystallized polymer by reducing the size of crystal part and disentanglement of amorphous chains. Among the observed fillers, small particles without surface modification possessed the most applicability and resulted in the smallest activation volume. However, other composites behaved with better $\eta_M$ while larger activation volume than neat matrix, which indicated that the mobility of these fillers in matrix became active compared to that of small particles without surface modification.

$\eta_M$ showed a clear dependence on stress and was explained by using Eyring stress-activated process. Although $\eta_M$ was not sensitive to temperature, there were, however, some interesting trends under each stress level, as shown in Fig. 7. In general, $\eta_M$ was increased with increasing temperature under 20 MPa except for PA/21-SM, in which $\eta_M$ was decreased at 80 °C, as illustrated in Fig. 7(a). The result indicates a fact that under low stress levels the permanent deformation of each specimen was reduced at elevated temperatures, which may be due to that small load could not activate many polymer segments or damage polymer structure permanently at high temperatures. Accordingly, the bulk materials were highly thermally activated other than stress activated at elevated temperatures and thus behaved with strong recoverable capability, which confirmed with decreased retardant time under 20 MPa, as shown in Table 2. However, under higher stress level, e.g., 40 MPa, advanced creep processes were stress activated, such as the slippage of crystallized polymer and the disentanglement of amorphous polymer, in a large scale of mobility with great irreversible deformation and large activation volume, as shown in Fig. 7(c) and Table 2, respectively. It was noteworthy to point out that in the case of 30 MPa $\eta_M$ showed an ambiguous dependence on temperature. $\eta_M$ at 80 °C was slightly changed compared to that at 23 °C for each specimen, however, obviously decreased to a very close value for all observed materials at 50 °C, as shown in Fig. 7(b). At 23 °C, since the materials were not thermally activated and the moderately low external stress was not able to make a pronounced creep process, the viscous flow was not obviously activated and was in relatively low level. However, at 80 °C, large instantaneous deformation resulted due to many thermally activated polymer chains under external stress. Therefore, the orientation of polymer chains occurred to a great extent and resulted in highly orientating hardening and crystallization in bulk materials [18,23]. Thereafter the advanced creep flow became much difficult and the resulting $\eta_M$ at 80 °C was very close to that at 23 °C. It was a different scene at 50 °C, at which materials began to enter the glass transition region and the amount of thermally activated chains was small. What was most important was the degree of the instantaneous deformation and orientation, which was very mild and led to low orientation hardening compared to that at 80 °C. It indicated the materials had the potential to perform advanced viscous flow with increasing time under this condition. This was confirmed by the directly fitted creep rates [1], which were dominated by $\eta_M$ at large time scale according to Eq. (3).

### 4.2. Modeling parameters from Findley power law

The Burgers model provided a constitutive representative and the modeling parameters showed a detailed structure-to-property relationship of the polymer composites. Additionally, an empirical model, i.e., Findley power law, was frequently applied to simulate and predict the long-term creep properties due to its simple expression and satisfactory applicability [19]. Hereby this method was also adopted to provide a wide understanding of the creep performance of nanocomposites.

The simulated sample curves of specimens at 50 °C were illustrated as dash lines in Fig. 3 under 20 MPa (a), 30 MPa (b), and 40 MPa (c). It could be seen that the fitting curves agreed very well with the experimental data. Since the power $n$ of each specimen was not sensitive to stress, it was considered as constant at each temperature. The complete modeling parameters $\varepsilon_{F0}$, $\varepsilon_{F1}$ and $n$ under each condition are listed in Table 3, from which an explicit dependency both on stress and on temperature of the modeling parameters came into view. On the one hand, both the time-independent strain $\varepsilon_{F0}$ and time-dependent term $\varepsilon_{F1}$ showed obvious growth with increasing stress level at each temperature; on the other hand, it exhibited the same behavior that $\varepsilon_{F0}$ and $\varepsilon_{F1}$ were increased with increasing temperature under each stress level. However, the increasing amplitude of $\varepsilon_{F1}$ was quickly slowed down from 50 °C to 80 °C under stress below 30 MPa, which showed that $\varepsilon_{F1}$ was not sensitive to temperature under moderately low stress level. The behavior of $\varepsilon_{F0}$ was equivalent to the

Table 3
The simulated parameters of the Findley power law

| Sample | $\sigma_0$ (MPa) | 23 °C | | | 50 °C | | | 80 °C | | |
|---|---|---|---|---|---|---|---|---|---|---|
| | | $\varepsilon_{F0}$ (%) | $\varepsilon_{F1}$ ($10^{-4}$ $h^{1/n}$) | $n$ | $\varepsilon_{F0}$ (%) | $\varepsilon_{F1}$ ($10^{-4}$ $h^{1/n}$) | $n$ | $\varepsilon_{F0}$ (%) | $\varepsilon_{F1}$ ($10^{-4}$ $h^{1/n}$) | $n$ |
| PA66 | 20 | 0.312 | 15.0 | 0.296 | 1.826 | 143 | 0.0978 | 3.942 | 169 | 0.0658 |
| | 30 | 0.601 | 22.7 | | 2.249 | 317 | | 7.259 | 442 | |
| | 40 | 1.109 | 102.1 | | 6.222 | 573 | | 12.78 | 2380 | |
| PA/300 | 20 | 0.862 | 13.3 | 0.276 | 1.360 | 84.5 | 0.108 | 2.955 | 86.7 | 0.0848 |
| | 30 | 0.994 | 24.8 | | 1.834 | 188.4 | | 6.159 | 185 | |
| | 40 | 1.105 | 71.0 | | 4.173 | 394 | | 11.30 | 1280 | |
| PA/21-SM | 20 | 0.488 | 7.2 | 0.288 | 1.426 | 72.5 | 0.108 | 2.546 | 84.7 | 0.0896 |
| | 30 | 0.761 | 18.0 | | 1.678 | 171 | | 5.768 | 139 | |
| | 40 | 0.821 | 50.7 | | 3.044 | 307 | | 7.962 | 671 | |
| PA/21 | 20 | 0.349 | 8.9 | 0.276 | 1.038 | 82.6 | 0.103 | 2.078 | 109 | 0.0663 |
| | 30 | 0.498 | 19.9 | | 1.921 | 159 | | 4.756 | 231 | |
| | 40 | 0.610 | 48.2 | | 3.034 | 281 | | 7.415 | 722 | |
| PA/Clay | 20 | 0.446 | 9.8 | 0.302 | 1.122 | 109 | 0.111 | 3.175 | 87.2 | 0.0951 |
| | 30 | 0.566 | 18.9 | | 1.422 | 184 | | 6.112 | 209 | |
| | 40 | 0.695 | 54.6 | | 3.822 | 395 | | 10.81 | 1160 | |

instantaneous deformation $\varepsilon_{M1}$ of Burgers model in nature, where the representative parameter was the elasticity $E_M$ of the Maxwell spring. Additionally, the increment of $\varepsilon_{F0}$ and $\varepsilon_{F1}$ dependent on whatever temperature or stress were significantly reduced by the addition of nanofillers. In particular, PA/21 behaved with the minimum $\varepsilon_{F0}$ and $\varepsilon_{F1}$, and then PA/21-SM. PA/300 and PA/Clay were on the same level with slight enhancement compared to that of matrix PA66. The feature of $\varepsilon_{F0}$ was also coincident with that of $E_M$ as discussed above.

In addition, according to Eq. (7), the fitting curves of log strain difference (creep strain $\varepsilon_F$ − instantaneous strain $\varepsilon_{F0}$) vs. log time $t$ for PA and PA/21 under various stress levels are provided in Fig. 8 at 23 °C (a), 50 °C (b), and 80 °C (c). It could be seen that the fitting curves of each specimen were parallel and agreed very well with the experimental data, especially over large time scale, which indicated that the power $n$ was independent of stress and state of stress. From the figures it could also be obtained that the power $n$ of PA/21 was almost the same as that of PA66 at 23 °C while slightly higher than that of PA66 at elevated temperatures. This phenomenon implied that the nanofillers applied in this study could not affect the parameter $n$ so much, as shown in Table 3.

It could also be found from the curves in Fig. 8 that in the first several hours the fitting lines, however, were not coinciding well with the experimental data. This case might be due to the restriction of the loading system of the creep machine, by which the specimen was loaded to reach up to the desired stress asymptotically after sometime [25] and the experimental creep strain in the beginning stage was smaller than the real one. The numbers on the left in Fig. 8 indicated the strain at 1 h. To determine the strain represented by the curves, shift vertical scale to match this number.

### 4.3. Creep rates

Both the constitutive Burgers model and empirical Findley power law could be fitted to the experimental strain very well. In addition, another important parameter, creep rate, was also necessary to describe the creep characteristics. The complete creep rates at creep time equal to 200 h obtained from Burgers model ($\dot{\varepsilon}_B$) and Findley power law ($\dot{\varepsilon}_F$) were listed in Table 4 for each specimen. Comparatively, the directly fitting creep rates ($\dot{\varepsilon}_{II}$) from the secondary creep stage were provided there as well. It could be found from the table that $\dot{\varepsilon}_B$ and $\dot{\varepsilon}_F$ were very close to $\dot{\varepsilon}_{II}$ and showed the same dependency on both temperature and stress as $\dot{\varepsilon}_{II}$, which was already discussed in the Part I of the study [1].

However, the detailed creep rate values of these two models indicated their intrinsic characteristics. In general, $\dot{\varepsilon}_F$ was less than $\dot{\varepsilon}_B$ for each specimen under each condition. At room temperature, both $\dot{\varepsilon}_B$ and $\dot{\varepsilon}_F$ were slightly lower than $\dot{\varepsilon}_{II}$, showing the same applicability of the two models at ambient temperature. At the elevated temperatures, $\dot{\varepsilon}_B$ was gently larger than $\dot{\varepsilon}_{II}$ while $\dot{\varepsilon}_F$ fairly lower than $\dot{\varepsilon}_{II}$ for each specimen. This case hinted that the Burgers model was capable and precise enough to characterize the experimental data of nanocomposites, whereas the Findley power law was applicable to describe the creep behaviors that did not exhibit a pronounced secondary stage, especially over large time scale at temperatures above $T_g$. Their intrinsic difference could result in distinct capability to predict the long-term performance via short-term experiments, which would be discussed in the following section.

## 5. Prediction of long-term properties of nanocomposites

### 5.1. Prediction by both models

Both Burgers model and Findley power law are very widely applied to describe the creep behaviors of a number of different plastics, laminated plastics, wood, concrete and some metals as well [19]. Thereafter as an example we provided the prediction of creep strains of PA66, PA/300, and PA/21. Data for these experiments and constants corresponding to

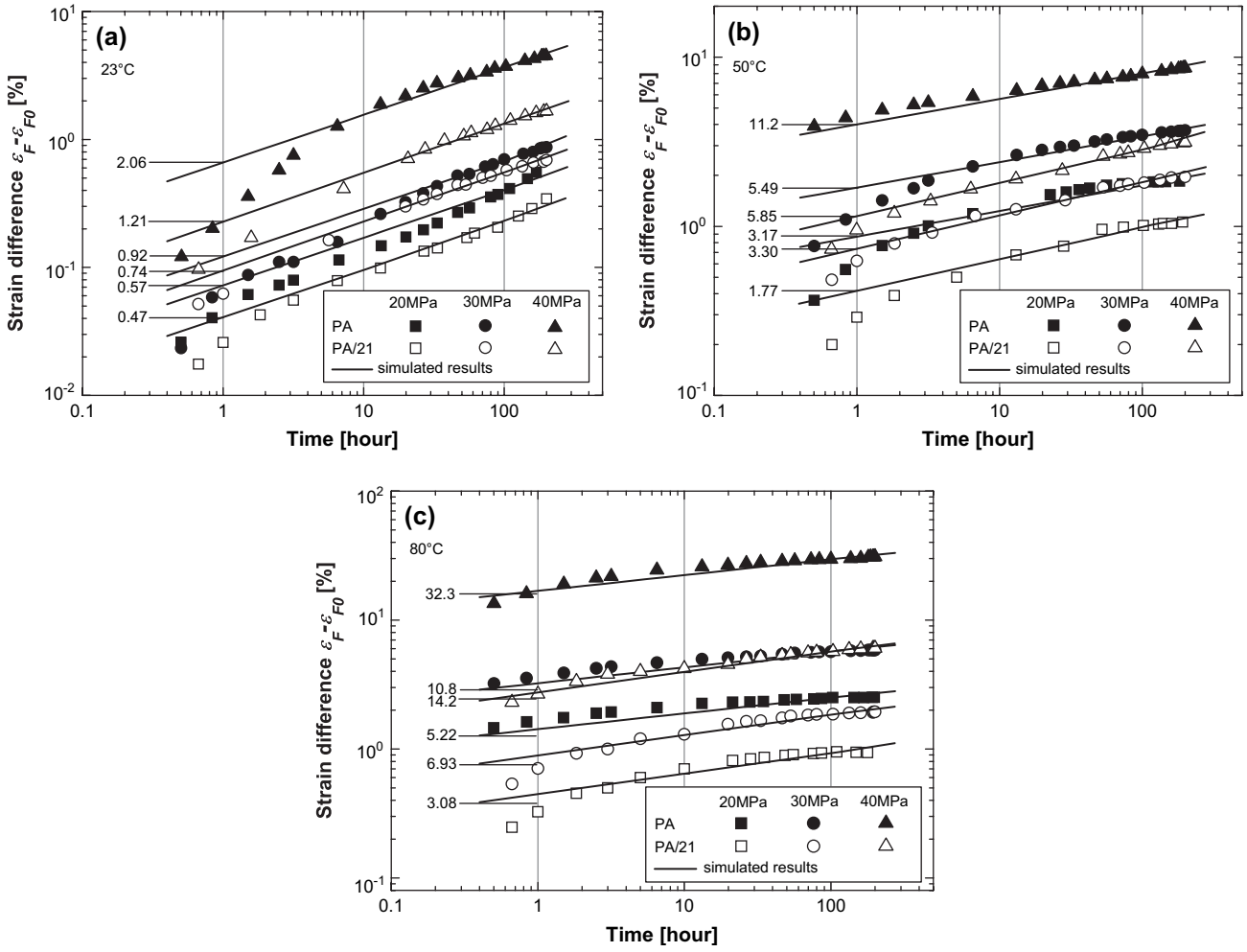


Fig. 8. Log strain difference $\varepsilon_F - \varepsilon_{F0}$ vs. log time $t$ for PA and PA/21 at (a) 23 °C, (b) 50 °C, and (c) 80 °C. (Note: numbers on left indicate strain at 1 h. To determine strain, shift vertical scale to match this number.)

Table 4
Comparison of the creep rates obtained from different models and direct linear regression

| Sample | $\sigma_0$ (MPa) | 23 °C ($10^{-6}$/h) | | | 50 °C ($10^{-6}$/h) | | | 80 °C ($10^{-6}$/h) | | |
|---|---|---|---|---|---|---|---|---|---|---|
| | | $\dot{\varepsilon}_B$ | $\dot{\varepsilon}_F$ | $\dot{\varepsilon}_{II}$ | $\dot{\varepsilon}_B$ | $\dot{\varepsilon}_F$ | $\dot{\varepsilon}_{II}$ | $\dot{\varepsilon}_B$ | $\dot{\varepsilon}_F$ | $\dot{\varepsilon}_{II}$ |
| PA66 | 20 | 22.5 | 10.7 | 22.6 | 13.4 | 11.7 | 8.01 | 11.9 | 7.88 | 4.79 |
| | 30 | 30.3 | 16.1 | 24.3 | 42.5 | 26.0 | 34.6 | 36.7 | 20.6 | 26.6 |
| | 40 | 99.0 | 72.5 | 103 | 93.2 | 47.0 | 88.3 | 193 | 111 | 137 |
| PA/300 | 20 | 15.7 | 7.92 | 16.4 | 8.90 | 8.09 | 8.06 | 6.17 | 5.76 | 1.68 |
| | 30 | 22.9 | 14.8 | 19.1 | 31.4 | 18.0 | 26.3 | 16.9 | 12.3 | 10.6 |
| | 40 | 58.7 | 42.3 | 61.2 | 70.2 | 37.7 | 68.3 | 124 | 85.1 | 111 |
| PA/21-SM | 20 | 8.35 | 4.77 | 8.63 | 6.75 | 6.94 | 4.36 | 9.32 | 6.10 | 2.35 |
| | 30 | 15.6 | 11.9 | 16.7 | 33.1 | 16.4 | 30.0 | 13.8 | 10.0 | 9.25 |
| | 40 | 44.6 | 33.6 | 47.4 | 51.7 | 29.4 | 50.7 | 69.8 | 48.3 | 65.8 |
| PA/21 | 20 | 11.0 | 5.30 | 11 | 8.18 | 7.34 | 6.84 | 5.48 | 5.13 | 1.68 |
| | 30 | 16.3 | 11.9 | 17.7 | 25.7 | 14.1 | 21.3 | 15.2 | 10.9 | 21.3 |
| | 40 | 38.7 | 28.7 | 42.9 | 40.5 | 25.0 | 39.8 | 50.4 | 34.0 | 45.6 |
| PA/Clay | 20 | 15.0 | 7.33 | 15.2 | 13.7 | 10.9 | 12.1 | 10.0 | 6.86 | 11.2 |
| | 30 | 23.0 | 14.1 | 17.1 | 28.8 | 18.4 | 25.6 | 24.2 | 16.4 | 16.3 |
| | 40 | 57.5 | 40.8 | 63.7 | 73.5 | 39.5 | 73.0 | 125 | 91.3 | 122 |

The creep rates $\dot{\varepsilon}_B$ and $\dot{\varepsilon}_F$ are calculated by using Findley power law and Burgers model, respectively, at time $t = 200$ h. $\dot{\varepsilon}_{II}$ is directly fitted from the secondary creep stage in the creep strain vs. time curve [1].

Eqs. (2) and (5) were determined from the first 100 h creep. The tests, however, were continued uninterrupted for roughly 360 h. Subsequently, these data were compared with predictions from Eqs. (2) and (5) based on the constants previously determined. The results were shown in Fig. 9. Although the modeling curves agreed very well with the experimental data within the applied time period, i.e., 100 h, it could obviously be seen over that period the prediction of the Findley power law was very satisfactory and that of the Burgers model, however, showed a huge deviation from the experimental data. Hence, the accuracy with which a creep equation describes the time dependence becomes an important consideration. Therefore, it is necessary and useful to analyze the difference between the creep models applied in this study in order to obtain a deep understanding in nature.

According to the above simulation results, these two models could describe the creep behavior satisfactorily in terms of both creep strain and creep rate within the experimental time range. Additionally, considering Eq. (3), the creep rate

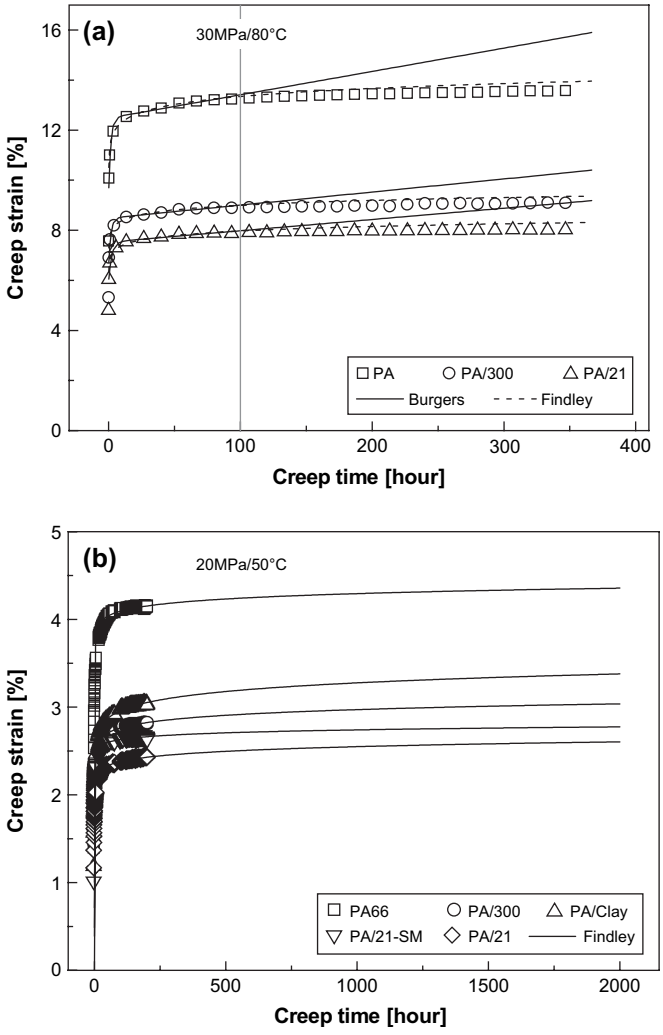


Fig. 9. Prediction by using creep models: (a) comparison of the predicting ability of the Burgers model and Findley power law for PA and the nanocomposites under 30 MPa/80 °C; (b) the application of Findley power law to predict the creep deformation of PA and the nanocomposites under 20 MPa/50 °C in 2000 h based on the 250 h experimental data.

of the Burgers model was dominant with $\eta_M$ and $\eta_K$, while the contribution of the latter was greatly controlled by the value of $e^{-t/\tau}$. When the creep time was relatively long, e.g., 100 h in the current study, $\tau$ was calculated less than 10 h at 80 °C. Thus, $e^{-t/\tau}$ was about $10^{-5}$ and Eq. (3) could be approximated to Eq. (4), which indicated the creep rate was thereafter constant and totally controlled by the permanent viscous flow $\eta_M$. However, the inner structures of the materials became much complicated due to the cooperative influences of stress and elevated temperature with increasing time, which implied that $\eta_M$ was highly time-dependent and could not be used to represent the future behavior. Comparatively, the creep rate equation deduced with time from the Findley power law might imply a true case that the thermoplastic nanocomposites behaved with a non-pronounced secondary creep stage and therefore it was satisfactory to predict the creep characteristics over a large time scale [18,19].

As an example, the Findley power law was applied to predict the long-term creep behavior of PA and nanocomposites. The prediction was executed up to 2000 h based on the 250-h experimental data, as shown in Fig. 9(b). It confirms that the power law displays very good predicting performance, which is widely applied in engineering applications [19]. From the predicted curves, it was found that the creep resistance of nanocomposites was also obviously enhanced compared to that of neat matrix even at long-term scale, which confirms with the short-term experiments.

### 5.2. Prediction by the time–temperature superposition method

The analysis in the former subsection confirmed that the Findley power law was a satisfactory means to predict the long-term creep performance. Furthermore, we would like to provide another method, i.e., time–temperature superposition principle, to observe the long-term property of nanocomposites. The creep strains were measured at 23, 40, and 50 °C, respectively, under a constant load of 15 MPa for appropriate time scale to make sure of the strain overlap at neighboring temperatures. The sample curves of PA66 and PA/21 were presented as creep compliance in Fig. 10(a). It could also be seen that both the creep compliance and creep rate were significantly reduced in PA/21 at each temperature. The sample master creep compliance curves of three materials were illustrated in Fig. 10(b). The master curves were extended up to $10^{10}$ s in time scale. The creep compliance of PA/21 was obviously lower than that of PA, which showed the reinforcing effectiveness of nanoparticles. The increment of compliance with time was slowed down from $10^9$ to $10^{10}$ s, showing the materials entered into a rubbery state [21] over an extremely long period of time. The viscoelastic stage data were simulated by using Eq. (6) and the resulting curves satisfactorily agreed with the master creep data. The reduced parameters were obtained and given in Table 5.

The shift factor showed a good linear dependence on the temperature, as given in Fig. 10(b) with insertion graph. The activation energy was obtained by the slope of a plot of log $a_T$

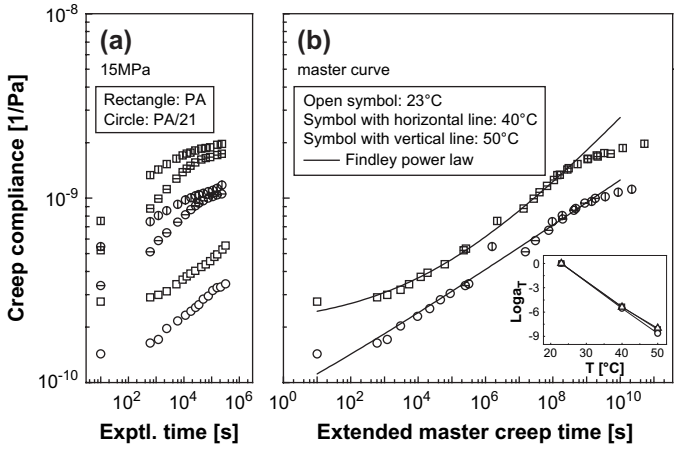


Fig. 10. The application of time–temperature superposition method: (a) creep compliance of PA66 and PA/21 obtained under 15 MPa at 23 °C, 40 °C, and 50 °C, respectively; (b) master creep compliance curves of the tested specimens at a reference temperature of 23 °C with the Findley power law simulating results. The insertion graph shows the shift factor, log $a_T$, as a function of temperature.

Table 5
The simulated Findley power law parameters and activation energy of the specimens obtained from the master curves

| Specimen | $J_{F0}$ ($\times 10^{-10}$ Pa$^{-1}$) | $J_{F1}$ ($\times 10^{-10}$ Pa$^{-1}$ h$^{1/n}$) | $n$ | $\Delta H$ (kJ/mol) |
|---|---|---|---|---|
| PA | 1.996 | 0.280 | 0.1957 | 553.3 |
| PA/300 | 1.947 | 0.339 | 0.1512 | 585.6 |
| PA/21-SM | 1.439 | 0.286 | 0.1628 | 616.0 |
| PA/21 | 0.178 | 0.704 | 0.1244 | 545.0 |
| PA/Clay | 0.508 | 0.822 | 0.1174 | 590.2 |

against $1/T$, as expressed in Eq. (14). The calculated values are listed in Table 5. The activation energy of the nanocomposites except for PA/21 was higher than that of PA66, which, together with the reduced activation volume at 50 °C obtained in Table 2, indicated that the immobilization of polymer chains became much difficult due to the addition of nanofillers. However, in the case of PA/21 although the activation energy was very close to that of matrix, the small nanoparticles still exhibited the reinforcing effect because a considerable reduction of the activation volume had resulted due to their presence.

## 6. Conclusions

In the current study the modeling of creep deformation of PA66 and its nanocomposites were satisfactorily conducted by using Burgers model and Findley power law. The simulating parameters helped to comprehensively understand the creep resistant composites by the addition of nanofillers and suggested the structure–property relationship representatively. Additionally, the long-term behavior was predicted by using the Findley model and time–temperature superposition method. The major results in this work could be concluded:

I. For the Burgers model, the instantaneous modulus $E_M$, the retardant modulus $E_K$ and viscosity $\eta_K$ showed an explicit dependence on temperature and stress, which also indicated a fact that the materials behaved with higher stiffness and lower deformability under long-term loading situation due to the addition of nanofillers. The permanent viscosity $\eta_M$ exhibited an implicit dependence on temperature and stress, showing a complicated combination of stress and thermally activated processes. The nanofillers generally contributed to the improved $\eta_M$ and thus resulted in reduced creep deformation and creep rate.

II. For the Findley power law, the modeling parameters $\varepsilon_{F0}$ and $\varepsilon_{F1}$ enhanced with increasing temperature and stress. The power $n$ of each material was independent on the stress level at constant temperature while decreased with increasing temperature. The nanocomposites behaved with the low simulating values compared to neat matrix, showing the reinforcing effectiveness by the addition of nanofillers, especially in the case of small particles.

III. Both the constitutive Burgers model and the empirical Findley power law could satisfactorily describe the creep strain and creep rate. However, the Findley power law was of the good predicting ability over large time scale. The master curves constructed by using the time–temperature superposition principle greatly extended the creep behavior over 11 decades of time. The creep resistance of the nanocomposites was obviously enhanced compared to that of neat matrix as well.

IV. The activation volume obtained from the Eyring process for the nanocomposites was decreased at each temperature, implying the enhanced immobility of polymer chains due to the presence of nanofillers. The increased activation energy obtained from TTSP indicated that the creep process needed much work for a quite local motion of polymer segments. Both activation volume and activation energy suggested the reinforcing influence of the nanofillers on the immobility of polymer chains.

V. Among the nanofillers, small nanoparticles behaved with the best capability to improve the creep resistance probably due to the dense and stiff network formed between particles and bridging segments to retard and restrict the mobility of polymer chains. Surface modification might improve the dispersion of nanoparticles, but reduce the interfacial strength thus to discount the enhancement of creep resistance. Comparatively, the sparse network in large particles was not effective to restrain the mobility of polymer in contrast with the dense network of small particles. Although nanoclay have large aspect ratio, the slippage of non-exfoliated and aggregated clay stacks under shear stress due to viscous flow of matrix compromised their reinforcement and resulted in a similar performance as large particles in our study.

## Acknowledgements

Z. Zhang is grateful to the Alexander von Humboldt Foundation for his Sofja Kovalevskaja Award, financed by the German Federal Ministry of Education and Research (BMBF)

within the German Government's 'ZIP' program for investment in the future. Additional thanks are due to FACT GmbH for the cooperation of composite injection molding.

## References

[1] Yang J-L, Zhang Z, Schlarb A, Friedrich K. On the characterization of tensile creep resistance of polyamide 66 nanocomposites. Part I: experimental results and general discussions. Polymer 2006;47:2791–801.
[2] Odegard GM, Gates TS, Nicholson LM, Wise KE. Equivalent-continuum modeling of nano-structured materials. Compos Sci Technol 2002; 62:1869–80.
[3] Finegan IC, Tibbetts GG, Gibson RF. Modeling and characterization of damping in carbon nanofiber/polypropylene composites. Compos Sci Technol 2003;63:1629–35.
[4] Gates TS, Odegard GM, Frankland SJV, Clancy TC. Computational materials: multi-scale modeling and simulation of nanostructured materials. Compos Sci Technol 2005;65:2416–34.
[5] Hu N, Fukunaga H, Lu C, Kameyama M, Yan B. Prediction of elastic properties of carbon nanotube reinforced composites. Proc Roy Soc A Math Phys Eng Sci 2005;461:1685–710.
[6] Sheng N, Boyce MC, Parks DM, Rutledge GC, Abes JI, Cohen RE. Multiscale micromechanical modeling of polymer/clay nanocomposites and the effective clay particle. Polymer 2004;45:487–506.
[7] Tseng KK, Wang LS. Modeling and simulation of mechanical properties of nano-particle filled materials. J Nanopart Res 2004;6:489–94.
[8] Odegard GM, Clancy TC, Gates TS. Modeling of the mechanical properties of nanoparticle/polymer composites. Polymer 2005;46:553–62.
[9] Schultz AJ, Hall CK, Genzer J. Computer simulation of block copolymer/nanoparticle composites. Macromolecules 2005;38:3007–16.
[10] Valavala PK, Odegard GM. Modeling techniques for determination of mechanical properties of polymer nanocomposites. Rev Adv Mater Sci 2005;9:34–44.
[11] Garces JM, Moll DJ, Bicerano J, Fibiger R, McLeod DG. Polymeric nanocomposites for automotive applications. Adv Mater 2000;12:1835–9.
[12] Hong CH, Lee YB, Bae JW, Jho JY, Nam BU, Hwang TW. Preparation and mechanical properties of polypropylene/clay nanocomposites for automotive parts application. J Appl Polym Sci 2005;98:427–33.
[13] Sarvestani AS, Picu CR. Network model for the viscoelastic behavior of polymer nanocomposites. Polymer 2004;45:7779–90.
[14] Blackwell RI, Mauritz KA. Mechanical creep and recovery of poly(styrene-*b*-ethylene/butylene-*b*-styrene)(SEBS), sulfonated SEBS (sSEBS), and sSEBS/silicate nanostructured materials. Polym Adv Technol 2005;16:212–20.
[15] Zhang Z, Yang J-L, Friedrich K. Creep resistant polymeric nanocomposites. Polymer 2004;45:3481–5.
[16] Yang J-L, Zhang Z, Zhang H. The essential work of fracture of polyamide 66 filled with $TiO_2$ nanoparticles. Compos Sci Technol 2005;65: 2374–9.
[17] Zhang H, Zhang Z, Yang J-L, Friedrich K. Temperature dependence of crack initiation fracture toughness for polyamide nanocomposites. Polymer 2006;47:679–89.
[18] Yang J-L. Doctoral dissertation: characterization, modeling and prediction of the creep resistance of polymer nanocomposites. Kaisersluatern: IVW; 2006.
[19] Findley WN, Lai JS, Onaran K. Creep and relaxation of nonlinear viscoelastic materials: with an introduction to linear viscoelasticity. New York: Dover Publications, Inc; 1989.
[20] Schapery RA. Nonlinear viscoelastic and viscoplastic constitutive equations based on thermodynamics. Mech Time-Depend Mater 1997;1:209–40.
[21] Ward IM. Mechanical properties of solid polymers. Weinheim: John Wiley and Sons Ltd; 1983.
[22] Williams ML, Landel RF, Ferry JD. The temperature dependence of relaxation mechanisms in amorphous polymers and other glass-forming liquids. J Am Chem Soc 1955;77:3701–7.
[23] Harren SV. Toward a new phenomenological flow rule for orientationally hardening glassy-polymers. J Mech Phys Solids 1995;43:1151–73.
[24] Wilding MA, Ward IM. Creep and recovery of ultra high modulus polyethylene. Polymer 1981;22:870–6.
[25] User's manual of creep rupture test machine – Model 2002. Dortmund: COESFELD GmbH and Co. KG; 2002.